



## Three-dimensional effects during thermocapillary-driven melting of PCMs in cuboidal containers in microgravity

B. Šeta<sup>a,\*</sup>, P. Salgado Sánchez<sup>b</sup>, D. Dubert<sup>c</sup>, J. Massons<sup>c</sup>, Jna Gavaldà<sup>c</sup>, J. Porter<sup>b</sup>, M. Mounir Bou-Ali<sup>d</sup>, X. Ruiz<sup>c</sup>, V. Shevtsova<sup>d,e</sup>

<sup>a</sup> Department of Civil and Mechanical Engineering, Technical University of Denmark, Kongens Lyngby, Denmark

<sup>b</sup> Center for Computational Simulation, Escuela Técnica Superior de Ingeniería Aeronáutica y del Espacio, Universidad Politécnica de Madrid, Madrid, Spain

<sup>c</sup> Facultat de Química, Universitat Rovira i Virgili, Tarragona, Spain

<sup>d</sup> Mechanical and Manufacturing Department, Mondragon University, Mondragon 20500, Spain

<sup>e</sup> Ikerbasque, Basque Foundation for Science, Bilbao, Spain

### ARTICLE INFO

#### Keywords:

Phase change materials  
Thermocapillary effect  
Melting  
Microgravity

### ABSTRACT

The melting of a phase change material (PCM) in a cuboidal domain under microgravity conditions is investigated numerically. The upper surface of the PCM is free (in contact with air, for example) and variations in its surface tension drive thermocapillary convection in the liquid phase, which significantly enhances heat transfer and accelerates melting. Furthermore, the change in liquid fraction during melting is associated with transitions among various modes of thermocapillary dynamics, including an oscillatory instability to hydrothermal waves. While the characteristics of PCM melting and thermocapillary dynamics have previously been investigated in this system using a two-dimensional model, the current work examines the important question of transverse dynamics and their effect on the melting process. Careful quantitative comparisons are made between the three- and two-dimensional models in terms of melting times, solid/liquid interface evolution, thermal fields, and spectrograms. The results show that transverse modes are often, but not always, reflection symmetric about the midplane and that their influence on melting and PCM performance is relatively minor in most cases. Thus, two-dimensional models may be used to reduce computational costs while still providing a reasonable approximation of the melting process for high Prandtl number materials, especially when compared to the midplane of the full cuboidal domain.

### 1. Introduction

Phase Change Materials (PCMs) are used in a wide range of applications [1–5] to manage temperatures and improve efficiency. Most common PCM devices are based on the solid/liquid phase transition; they absorb excess heat as they melt and release it again during solidification. In this way, PCMs increase the thermal inertia of the system, moderating extreme temperatures and storing (recycling) energy that would otherwise be lost. The performance of a PCM device depends on this capacity to store energy, which is principally determined by the latent heat of fusion, on the temperature at which the phase change occurs, and on its ability to absorb and transfer energy to the external environment (or the relevant thermally coupled device).

There is a wide variety of PCMs to select from in most applications including organic materials, typified by alkanes, and inorganic

materials, typified by hydrated salts. Both these classes of PCMs have broadly similar costs, offer comparable energy storage capacities [6] (with salt hydrates having a moderate advantage here) and a range of convenient melting temperatures. However, inorganic salts often suffer from chemical instability, concerns about corrosion or toxicity, and large supercooling effects (unreliable melting temperatures). Organic PCMs are therefore more attractive for applications requiring greater chemical stability or with more demanding safety constraints.

Nonetheless, one of the most notable disadvantages of organic PCMs is their relatively low thermal conductivity, which makes them less responsive to rapid thermal changes. Increasing the rate at which they can absorb and release heat is thus a key focus for performance enhancement that has motivated several different design strategies. Most obviously, the design of the PCM device can be modified to incorporate more conducting materials like metal fins [7] or to include

\* Corresponding author.

E-mail address: [berse@dtu.dk](mailto:berse@dtu.dk) (B. Šeta).

an active heat transfer loop that distributes heat or extracts it from the PCM [8,9].

There are certain applications, however, where the energy consumption of active heat transfer strategies or the increased size and mass of metal fins or similar material additions would not be desirable. One such application — the one of primary interest here — is in space exploration, where both energy costs and spacecraft/payload mass are to be minimized as much as possible. Spacecraft often endure large variations in temperature that can be detrimental to electronics and other systems, while manned missions also have critical thermal requirements for life support systems. PCM devices have a long history of use in the space industry going back to Apollo 15, Skylab SL-1, and the Venera 8–10 probes and may be expected to play an important role in the next phase of space exploration [10].

There are a couple of interesting passive strategies that present themselves as potential solutions to the problem of low heat transfer rates with organic PCMs that do not noticeably increase the mass of the device (alternatively, reduce its energy storage density). One of these involves the addition of nanoparticles, which can increase the thermal conductivity of the liquid and increase diffusive heat transfer [11,12]. The other strategy, which we focus on here, is to induce convection in the liquid phase during the melting or solidification process. In the presence of gravity, the buoyant force resulting from thermal expansion naturally drives convection and this is known to substantially reduce the melting time, especially when the PCM is heated from below. Following the experiments of Gau and Viskanta [13], there has been steady interest in the effect of buoyant convection on the phase change process [14–17].

In space applications, however, the PCM device must also operate effectively in reduced-gravity or microgravity environments where buoyancy is ineffective. It is with such applications in mind that the thermocapillary force has been investigated as an alternative for driving convective flow [18–20,21,22,23–29]. The thermocapillary (or thermal Marangoni) effect is one of the principle mechanisms behind a variety of important interfacial phenomena and occurs in the presence of a temperature gradient, which induces a surface tension gradient that draws fluid from (typically, warmer) areas of low surface tension to (typically, cooler) regions of higher surface tension. The associated convective flow can substantially improve heat transfer during melting and is independent of gravity. It requires a design with one or more free surfaces (liquid/gas interfaces) but is otherwise inherent to the operation of PCM devices where thermal gradients are naturally present.

The dynamics of thermocapillary convection are of interest in their own right, with a variety of distinct modes having been observed including steady return flow, steady multicellular structures, hydrothermal traveling waves, oscillatory standing waves and thermal traveling waves [20,30,31,32–36]. The melting of a PCM in the presence of thermocapillary convection can be seen as a fluid dynamics problem with an evolving boundary since both the volume fraction and the shape of the liquid domain change continually over time. This changing liquid domain tends to induce transitions among different thermocapillary modes as the effective forcing (Marangoni number) and aspect ratio (domain shape) change [31,37]. The corresponding instabilities not only alter the fluid dynamics but any measurable quantity that is influenced by them, like the heat transfer rate. It is clearly important to locate and understand the fluid instabilities that appear when PCMs melt and their effect on its performance.

The efficacy of thermocapillary convection and complementary strategies like nanoparticles for improving PCM performance in microgravity environments will be directly evaluated by the “Effect of Marangoni Convection on Heat Transfer in Phase Change Materials” (MarPCM) project, which is planned for implementation by the European Space Agency (ESA) on the International Space Station (ISS) [38,39]. A range of numerical investigations have recently been conducted in support of this anticipated experiment and the questions it addresses, including an analysis of dynamical modes and their effect on

heat transport [18–20,31], melting with combined gravitational and thermocapillary convection [40,41], PCM melting in a liquid bridge configuration in microgravity [27,28,37,42,43], the influence of surface heat exchange [30,44,37], the effect of nanoparticles [45], and the coupling between thermocapillary flows and sloshing [46–50].

Due to the need to sweep parameters while avoiding prohibitive computational cost, the simulations of cuboidal PCM geometries conducted in the above references were simplified by assuming two-dimensional (2D) flow (i.e., using rectangular geometry). While this simplification is justified to a large extent by the high Prandtl number of n-octadecane [33,51] and other alkanes and by successful comparison with the microgravity results of the “Thermocapillary Effects in Phase Change Materials in Microgravity” (TEPiM) experiment conducted during the 65th ESA Parabolic Flight Campaign [18,25,26], it is critical to make a direct and quantitative comparison with more realistic three-dimensional (3D) simulations in order to understand the influence of fluid dynamics in the transverse direction, particularly on the heat transfer rate. The aim of the present work is to provide such a quantitative comparison and to examine in detail the influence of the transverse dimension on the thermocapillary dynamics observed during the melting of a PCM.

The remainder of the paper is organized as follows. The numerical scheme behind the simulations is summarized in Section 2 including the selection of mesh sizes. The main results are presented in Section 3, which contains a detailed comparison of the 3D and 2D cases, including melting times, the movement of the solid/liquid front, thermal fields, and spectrograms for oscillatory flow. Three different PCM heights (aspect ratios) are considered.

## 2. Numerical scheme

Cuboidal domains of length  $L = 22.5$  mm, width  $W = 25$  mm, and heights  $H = 1.875, 2.5$  and  $3.75$  mm are used to resolve the 3D fluid dynamics of a melting PCM. The flow and temperature fields in the central plane of the container (see Fig. 1) are then compared with results obtained with a simplified 2D model. The longitudinal and transverse aspect ratios,  $\Gamma_L = L/H$  and  $\Gamma_W = W/H$ , are used to characterize the size of the PCM in the 3D simulations while, in the 2D case, there is a single aspect ratio  $\Gamma = \Gamma_L = L/H$ . N-octadecane is selected as the PCM due to the availability of reliable measurements of its thermophysical properties in the literature [12,52,53] and its relevance to recent experiments conducted in reduced gravity environments [18,25,26]. Table 1 lists the parameter values used in the simulations below.

Weightless conditions are assumed in all calculations and the flow of the liquid is considered to be laminar and incompressible, with constant thermophysical properties within the range of temperatures considered.

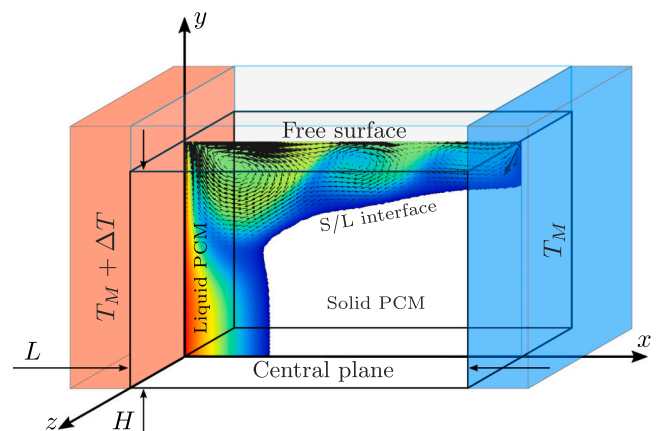


Fig. 1. Sketch of the 2D ( $xy$ -plane) and 3D domain used in calculations. A typical solid/liquid (S/L) interface is shown.

**Table 1**  
Physical properties of n-octadecane (C<sub>18</sub>H<sub>38</sub>), reproduced from [12,52,53]).

Solid phase	Density	$\rho_s$	865 kg/m <sup>3</sup>
	Specific heat capacity	$c_{ps}$	1934 J/(kg K)
	Thermal conductivity	$k_s$	0.358 W/(m K)
	Specific latent heat	$L_f$	243.5 kJ/kg
	Melting temperature	$T_m$	28 °C
Liquid phase	Density	$\rho_l$	780 kg/m <sup>3</sup>
	Dynamic viscosity	$\mu_l$	3.54 mPa s
	Specific heat capacity	$c_{pl}$	2196 J/(kg K)
	Thermal conductivity	$k_l$	0.148 W/(m K)
	Surface tension at $T_m$	$\sigma_0$	27.54 mN/m
	Thermocapillary coeff.	$\gamma$	$8.44 \times 10^{-5}$ N/(m K)

The numerical simulations use a solid/liquid phase-change model based on the enthalpy-porosity formulation of the Navier-Stokes equations. This approach allows the solid/liquid (S/L) interface to be treated smoothly, without the need to explicitly track it throughout the process. Details on the formulation of the corresponding momentum and temperature balances can be found in the literature [54–56] and will only be summarized here. The momentum and continuity equations are

$$\frac{\partial \mathbf{u}}{\partial t} + (\mathbf{u} \cdot \nabla) \mathbf{u} = -\frac{\nabla p}{\rho_l} + \nu \nabla^2 \mathbf{u} + \frac{1}{\rho_l} \text{DS}, \quad (1)$$

$$\nabla \cdot \mathbf{u} = 0 \quad (2)$$

where  $\mathbf{u}$  is the velocity vector  $\mathbf{u} = (u, v, w)$ ,  $p$  is the buoyant pressure (difference between total and hydrodynamic),  $\rho_l$  is the liquid density at a reference temperature,  $\nu = \mu_l/\rho_l$  is the kinematic viscosity and DS is the Darcy source term, defined below in Eq. (6). The energy equation can be written as

$$\rho_0 c_p \left( \frac{\partial T}{\partial t} + \mathbf{u} \cdot \nabla T \right) = \nabla^2 (kT) - \text{ES} \quad (3)$$

where  $c_p$  and  $k$  are the weighted specific heat and thermal conductivity defined below in Eq. (5) and ES is a source term related to the phase change process and defined in Eq. (7).

The starting point of the enthalpy-porosity formulation is the definition of a scalar field  $f_l$  characterizing the local liquid fraction. This field depends on temperature and is bounded between zero (a pure solid) and unity (a pure liquid). It provides the coupling between the momentum and energy equations. To model the liquid fraction in regions with a (homogeneous) mixture of solid and liquid, which are the so-called mushy regions, a linear interpolation between the solidus temperature,  $T_s$ , and liquidus temperature,  $T_m$ , is used.

$$f_l = \begin{cases} 0 & T \leq T_s, \\ 1 & T \geq T_m, \\ \frac{T - T_s}{T_m - T_s} & T_s < T < T_m. \end{cases} \quad (4)$$

Here, we take  $T_m - T_s = \Delta T_s = 1$  K to be the size of the temperature interval defining the mushy region [18,19]. Physical properties are assumed to vary linearly between the limiting solid and liquid values:

$$(c_p, k) = (c_{ps}, k_s)(1 - f_l) + (c_{pl}, k_l)f_l. \quad (5)$$

The liquid fraction is included in the momentum balance via a Darcy source term, DS, that takes the form of a Carman-Kozeny equation,

$$\text{DS} = \frac{C(1 - f_l)^2}{\delta + f_l^3} \mathbf{u}. \quad (6)$$

If the control volume is completely liquid ( $f_l = 1$ ), the Darcy term vanishes and the usual Navier-Stokes equations hold. On the other hand, if the control volume is completely solid ( $f_l = 0$ ), the Darcy term becomes dominant and the velocity is approximately zero, ensuring that the solid does not move. If the control volume is in the mushy region

( $0 < f_l < 1$ ) containing a mixture of liquid and solid, the DS term is finite and modifies the Navier-Stokes equations. The resulting velocity field in this region is common to both solid and liquid phases since the mixture is assumed to be homogeneous, with the solid phase fully dispersed within the liquid. In this way, the Darcy term allows the momentum equation to be resolved over the entire computational domain without explicitly tracking the S/L interface.

The value of the permeability (or Darcy) coefficient  $C$  in the DS term has a strong influence on behavior in the mushy region. If the value of  $C$  is raised, for example, the flow in the mushy region is reduced, which leads to a corresponding reduction in convected heat and a flattening of the S/L front. Thus, the value of  $C$  should be adjusted based on experimental results to optimize the correspondence of the computational model. In general, the choice of this coefficient is related to the morphology of the selected PCM. In the present work, the value of  $C$  is set to  $1.6 \times 10^6$  kg m<sup>3</sup> s, while the constant  $\delta$ , which prevents division by zero, is set to  $10^{-3}$  [23,28,43].

The shape of the mushy region is controlled by the transport of enthalpy, so it is essential to solve the energy balance accurately. This balance, expressed in terms of temperature, involves another source term,

$$\text{ES} = \rho_l L_f \left( \frac{\partial f_l}{\partial t} + \mathbf{u} \cdot \nabla f_l \right). \quad (7)$$

For sufficiently narrow mushy regions, the effect of the advective term  $\mathbf{u} \cdot \nabla f_l$  can be neglected.

Appropriate boundary conditions must be defined in order to complete the formulation of the problem. Here, the longitudinal endwalls are considered to be no-slip for the flow and are held at constant but distinct temperatures. The right (cold) endwall at  $x = L$  has the fixed temperature  $T_m$  while the left (hot) endwall at  $x = 0$  is maintained at  $T_h = T_m + \Delta T$  with  $\Delta T = 20, 30$  or  $40$  K. The remaining solid walls are also considered to be no-slip for the flow but adiabatic for the temperature field. Such adiabatic boundary conditions are consistent with the previous 2D simulations [18–20,31] used for comparison. We note that resolving the entire 3D domain with the boundary conditions specified above is computationally expensive, but avoids a priori assumptions of symmetry. An assumption of transverse reflection symmetry  $z \rightarrow -z$ , for example, allows the computational domain to be halved but forfeits the possibility of observing solutions that break this symmetry.

The free surface on the top side is assumed to remain perfectly flat. This is consistent with the fact that the cells of the MarPCM experiment are specially designed to maintain the contact line by pinning it to a sharp edge of the container [39] and the value of the so-called capillary number,  $\text{Ca} = (\nu \Delta T)/\sigma_0$ , which determines the extent of the free surface deformation caused by the thermocapillary effect. In this case,  $\text{Ca} \leq 0.123$ , which indicates negligible free surface deformation [20,57]. Adiabatic thermal conditions are also imposed on this free interface so that no heat is transferred across it. Heat flux along the interface, however, is crucial to the problem [30,44] and results both from the longitudinal temperature gradient and the dependence of surface tension on this gradient, which drives thermocapillary flow. Thermocapillary flow accelerates heat transport here since it draws liquid from warmer regions of lower surface tension to cooler regions of higher surface tension. The balance between viscous and thermocapillary forces is imposed on the non-deformable surface as

$$\mu \frac{\partial \mathbf{u}}{\partial n} = \gamma \frac{\partial T}{\partial \tau} \quad (8)$$

where  $\partial/\partial n$  and  $\partial/\partial \tau$  are the derivatives in the normal and tangential directions.

Finally, the setup of the problem is completed by selecting appropriate initial conditions for the velocity and temperature fields. The initial temperature  $T_0$  is chosen to lie below the solidus temperature  $T_s$  to ensure that the PCM is initially in the solid state. The initial velocity is

therefore taken to be zero everywhere. Due to this last initial condition and the imposed temperature  $T_m$  at the cold boundary, there is an interface (defined by  $f_l = 0.5$ ) detected near this side in all simulations.

The OpenFOAM package is used to solve the problem defined above. This package uses the finite volume method, which has the advantage of ensuring conservation of mass and energy flux between control volumes even over long simulation times, as required here. The numerical solver uses second-order schemes for space and time discretization. The time step, initially set to 1 ms, is automatically limited when necessary by the maximum Courant-Friedrich-Lewy condition with a very restrictive value of 0.25. The momentum and continuity equations are solved using the PIMPLE algorithm, which is a blended scheme based on the PISO and SIMPLE algorithms that ensures the correct coupling between pressure and velocity. The temperature is calculated at each PIMPLE iteration using a special linearization of the discretized source term [58–61]. The final system of linear equations is solved using the generalized Geometric-Algebraic Multi-Grid (GAMG) method, with a tolerance of  $10^{-8}$  for pressure, velocity and temperature fields. The matrices are preconditioned using a diagonal incomplete-LU (asymmetric) DILU preconditioner. Lastly, we note that, to reduce computation time, all 3D simulations were parallelized by splitting the cuboidal geometry into eight or twelve individual volumes using the so-called Scotch domain decomposition [3]. The 2D simulations were fast enough that they did not require any parallelization strategy.

Details about the validation of the code, based on extensive comparisons with positive and negative surface tension systems as well as with the phase change of Gallium [13] in a rectangular cavity heated from one side, have already been reported [28,43]. For these convergence tests, the entire evolution of the liquid fraction was compared [19]. In the 2D case with  $\Gamma = 12$ , three different rectangular meshes were considered with elementary cell dimensions of  $0.225 \times 0.054$  (rough),  $0.011 \times 0.025$  (medium) and  $0.075 \times 0.019$  mm<sup>2</sup> (fine).

Fig. 2 shows the time dependence of the liquid fraction  $X_L$  observed for both the lowest (20K) and highest (40 K) temperature differences considered. The difference between the finest mesh and the other two is

shown as a percent value of the total liquid fraction over time and the total runtime required to reach a liquid fraction of one (full melting) is recorded. It can be seen that the medium resolution mesh, which reduces the runtime by a factor of approximately two, is still quite accurate, with a level of numerical error (compared to the finest mesh) below 1%, on average. Although the 2D simulations are relatively fast, the high computational cost of each 3D simulation, motivated selection of the rougher mesh. Using cells of size  $0.225 \times 0.054$  mm<sup>2</sup> (length  $\times$  height) significantly reduces computational time while providing acceptable results, with a numerical error of less than 3%, on average, in the most unfavorable case of  $\Delta T = 40$  K.

For the 3D simulations, the third dimension (width) of the elementary cell volume can be larger than the other two since the temperature gradients in this direction are not strong. After several tests, a value of 0.625 mm was selected as a suitable value for the 3D simulations, with an acceptable runtime. Thus, orthogonal parallelepipedic elementary cell volumes of  $0.225 \times 0.054 \times 0.625$  mm<sup>3</sup> are used in the 3D calculations for  $\Gamma_L = 12$ ,  $\Gamma_W \simeq 13.33$  and for  $\Gamma_L = 9$ ,  $\Gamma_W = 10$ . For  $\Gamma_L = 6$ ,  $\Gamma_W \simeq 6.67$ , on the other hand, graded grids in the vertical dimension are used. The motivation behind this approach is to maintain a manageable runtime by increasing the density of cells only in regions where it is necessary — in the present calculations, that is the region near the free surface where large gradients are present due to thermocapillary flow. The meshes for  $\Gamma_L = 6$  use a single expansion ratio of 1.27 in the vertical direction, while the remaining elementary cell dimensions are unchanged. In this way, the orthogonality of the elementary volumes is preserved and they are practically identical near the free surface.

### 3. Results

In addition to the longitudinal and transverse aspect ratios,  $\Gamma_L$  and  $\Gamma_W$ , the melting PCM problem depends on the Prandtl (Pr), Marangoni (Ma) and Stefan (Ste) numbers. These are summarized for the selected temperature differences  $\Delta T$  in Table 2. Although the effective characteristic length that enters into the determination of the Marangoni

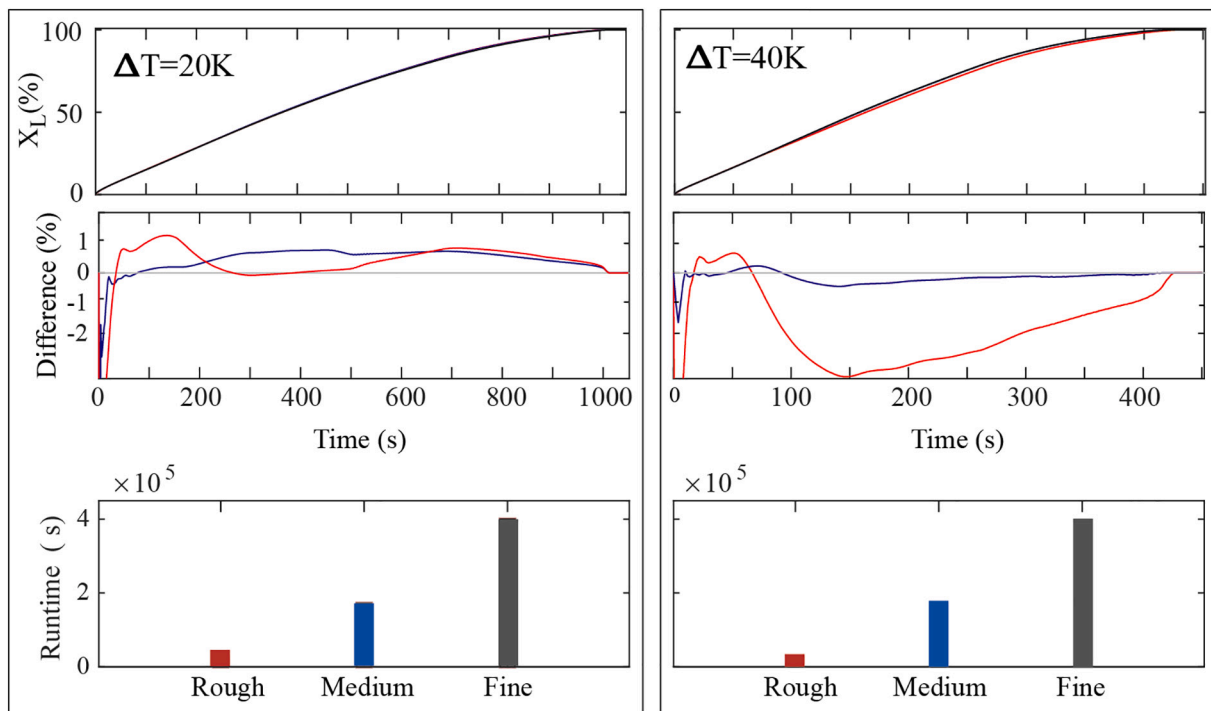


Fig. 2. Comparison of melting simulations using three different meshes in the 2D case with  $\Gamma = 12$ ,  $\Delta T = 20$  K (left) and  $\Delta T = 40$  K (right). The total liquid fraction (upper row) evolves similarly, with differences (middle row) of a few percent using the rough or medium meshes compared to the fine mesh but much reduced runtime (lower row).

**Table 2**

Characteristic Prandtl ( $Pr$ ), Marangoni ( $Ma$ ), and Stefan ( $Ste$ ) numbers associated with the simulations presented here.

$\Delta T$	20 K	30 K	40 K
$Pr = \frac{c_{pl}\mu_l}{k_l}$	52.5	52.5	52.5
$Ma = \frac{\gamma\rho_l c_{pl} L \Delta T}{\mu_l k_l}$	124,149	186,224	248,298
$Ste = \frac{c_{pl}\Delta T}{L}$	0.18	0.27	0.36

number may be considered to change with time due to the evolution of the S/L boundary during the melting process [31], the total length  $L$  of the domain is used here to obtain a constant  $Ma$ . This value is representative of the fully melted PCM and is less relevant for determining the early transitions (bifurcations) observed during the melting process itself. The various simulations in this section are, for that reason, characterized in terms of  $\Gamma_L$ ,  $\Gamma_W$  and  $\Delta T$ .

We remark that many of the computational results reported below focus on the thermal field because this information can more easily be extracted from experiments and used to test the validity of the results. Also, the numerical simulations are stopped at the end of the melting process and, thus, do not consider the possibility of additional dynamics or transitions occurring after that.

### 3.1. Melting dynamics

The evolution of thermocapillary dynamics during melting is considered here in terms of the thermal field and the S/L front for  $L = 22.5$  mm,  $W = 25$  mm, and three different values of the height  $H$ . PCM height is a key parameter for selecting the character of thermocapillary flow [20] and we take  $H = 3.75, 2.5$  and  $1.875$  mm, which correspond, respectively, to  $\Gamma_L = 6, 9$ , and  $12$ .

The evolution of the thermal field within the melting region is illustrated in Fig. 3 (videos available as supplementary material) using six vertical planes, three making longitudinal cuts and three making transverse cuts. The three longitudinal planes are located in the center  $z = 0$  and, symmetrically, at half the distance to each side  $z = \pm W/4$ . The locations of the transverse planes are chosen in order to provide good visualization during most of the melting process. The isotherms shown in the liquid have the same values on all planes. The S/L interface is shown as a (light) gray surface, which evolves and interacts with the flow and temperature fields.

During the first part of the melting process, the thermal field changes most rapidly near the free surface where the flow is dominated by thermocapillary forces. Below this surface region, the isothermal surfaces are relatively flat, indicating that conductive heat transport is more important in the region near the bottom boundary. The flow and thermal patterns are initially nearly independent of the  $z$  coordinate. The amount of liquid PCM continually increases while the S/L interface advances towards the cold side. The fact that it does this most rapidly near the free surface leads to an inclined, approximately flat shape.

The character of the thermocapillary flow changes when the oscillatory instability appears. The resulting hydrothermal waves have components in both the longitudinal and transverse directions. The movement of the isotherms in the longitudinal plane indicates intense variations near the hot side of the domain but, also, that the oscillatory dynamics do not appreciably modify the overall shape of the S/L front. For all three aspect ratios, the thermocapillary dynamics are initially symmetric with respect to the central plane (i.e., the fields are invariant under  $z \rightarrow -z$ ). Once they arise, hydrothermal waves persist throughout the remainder of the melting process [20]. However, in some cases — most notably for  $\Gamma_L = 12$  — these waves lose their transverse symmetry and begin to travel preferentially in one direction along the  $z$  axis. Note that they cannot be *pure* traveling waves due to the boundary conditions. We also emphasize that, since the applied temperature difference is

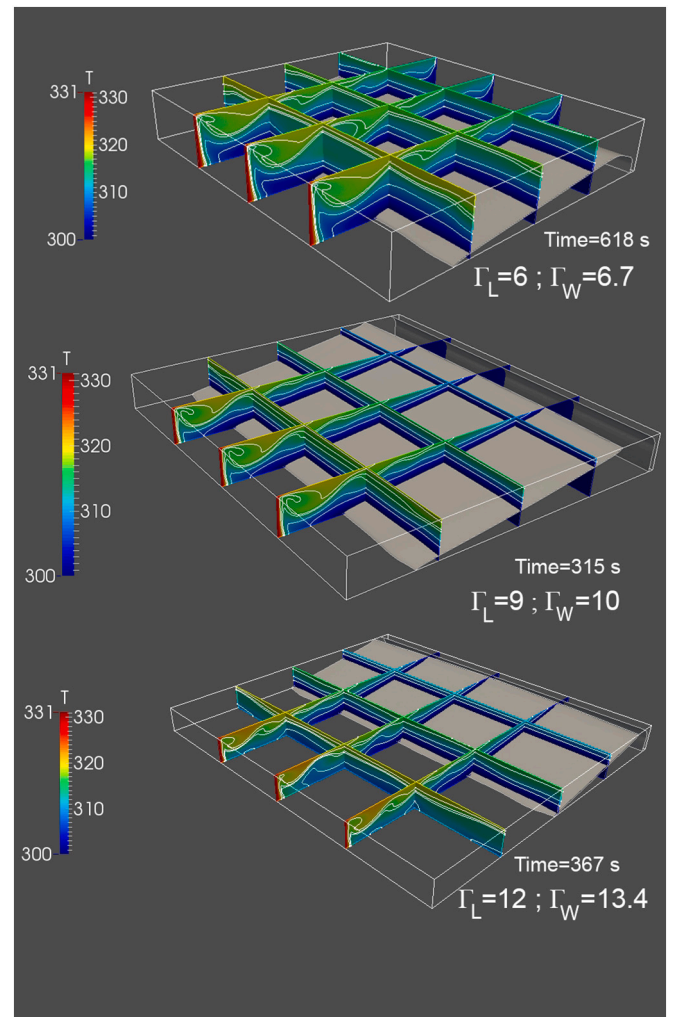


**Fig. 3.** Evolution of the liquid region and thermal field for  $\Delta T = 30$ K and (upper)  $\Gamma_L = 6$ , (middle)  $\Gamma_L = 9$ , (lower)  $\Gamma_L = 12$ .

constant, the observed instabilities are triggered by the changing volume, shape, and temperature distribution of the liquid phase as the PCM melts.

#### 3.1.1. Comparison of 3D and 2D melting times

Due to the importance of the increasing fraction of the liquid phase in selecting thermocapillary modes, Fig. 4 quantifies the changing liquid fraction in several ways and compares the 3D and 2D results. In particular, the upper part of Fig. 4 shows three characteristic times:  $t_{50}$ , at which 50% of the solid is melted,  $t_{surf}$ , at which the S/L front reaches the cold boundary and moves below the surface, and  $t_{end}$ , the complete melting time. Note that, due to the  $z$ -dependence of the S/L front (reminiscent of ripples) in some 3D simulations, the definition of  $t_{surf}$  is made using the profile from the central vertical plane at  $z = 0$ . The central row of Fig. 4 shows the time dependence of the total liquid fraction  $X_L$  for all 3D and 2D simulations, while the lower part complements this with its rate of change, which more clearly reveals certain features like the decrease in melting rate when the S/L front arrives at the cold boundary [27,41].

Different melting times  $t_{end}$  are observed for different aspect ratios, which correspond to different total volumes of PCM. However, if there were no thermocapillary convection and heat were transported solely by diffusion, then these melting times would be identical since, with fixed temperatures at  $x = 0$  and  $x = L$ , they would be determined only by the length  $L$  of the domain [19]. Here, the faster melting time for  $\Gamma_L = 12$  is

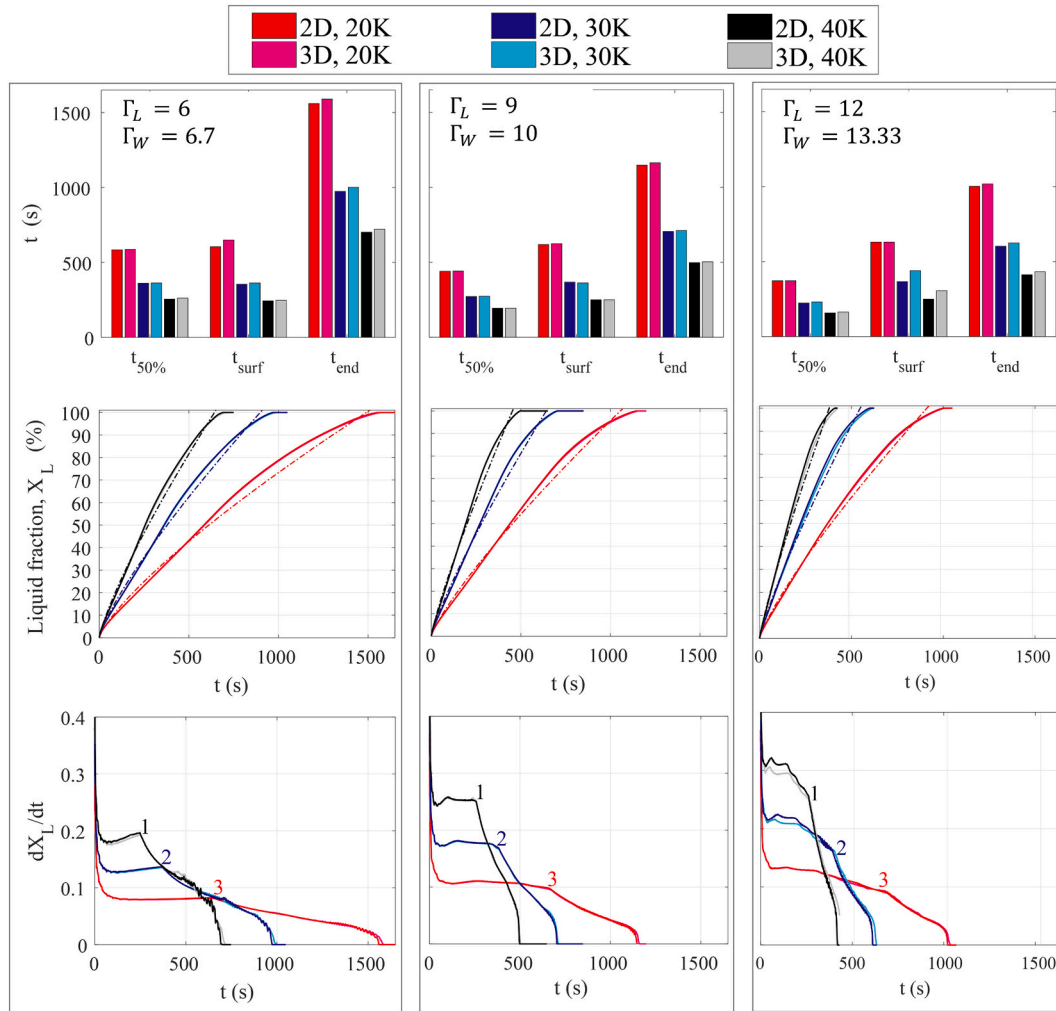


**Fig. 4.** Analysis of melting dynamics for  $\Delta T = 20, 30,$  and  $40$  K (color code in the legend) with  $\Gamma_L = 6$  (left column),  $9$  (center), and  $12$  (right), comparing the 3D and 2D cases. In many plots, the 3D and 2D results are nearly indistinguishable, especially those of the liquid fraction  $X_L$ ; the dash-dotted curves in those plots show fits with the  $t^{1/2}$  scaling of the one-dimensional two-phase Stefan problem (i.e., with no thermocapillary convection).

explained by the greater influence, compared to diffusion, of the thermocapillary flow, which is concentrated near the surface. The fact that melting time increases as  $\Gamma_L$  decreases below  $12$  ( $H$  is increased) is consistent with the 2D results of Salgado Sanchez et al. [19].

Despite the dependence of total melting time  $t_{end}$  on  $\Gamma_L$ , it is interesting to observe that the time  $t_{50}$  at which 50% of the solid is melted is approximately  $0.37 t_{end}$  for all aspect ratios. The more rapid melting for  $t < t_{50}$  is due to the greater influence of thermocapillary convection.

In contrast to  $t_{50}/t_{end}$ , the relative time required for the solid to disappear from the surface clearly depends on aspect ratio. If  $\Gamma_L = 12$ , the time  $t_{surf}$  is, on average, about  $0.67 t_{end}$  while for  $\Gamma_L = 9$  and  $\Gamma_L = 6$  it is approximately  $0.51 t_{end}$  and  $0.37 t_{end}$ , respectively. This dependence is explained by the fact that, as  $H$  increases, a greater percentage of the melting time is dependent on diffusive heat transfer as the S/L front slowly moves downward near the cold side of the container, away from the surface and its strong thermocapillary flow.

The total liquid fraction does not scale as  $t^{1/2}$ , as it would in the one-dimensional two-phase Stefan problem in a semi-infinite slab (see the dashed curves in the central row of Fig. 4). This is, of course, due to thermocapillary convection, which accelerates heat transfer and melting. It is instructive as well to look at the rate of change of this liquid fraction over time, as in Fig. 4(c). Independent of  $\Gamma_L$  and whether the simulation is 3D or 2D, this melting rate begins at a very high value (explained by the initially divergent temperature gradient) and then

stabilizes at a relatively constant value. Although there are smaller features in some cases, particularly with higher  $\Delta T$ , the main change occurs as the S/L front reaches the cold boundary at  $t_{surf}$ ; these times are labeled with 1, 2, and 3 for  $\Delta T = 20, 30$  and  $40$  K, respectively, in the figure. For  $t > t_{surf}$ , there is a notable decrease in the melting rate as the S/L front descends below the surface into a region of weaker thermocapillary flow.

Finally, note that in all cases the 3D and 2D melting times are quite similar. For example, the difference in  $t_{end}$  between the 3D case with  $\Delta T = 40$  K and  $\Gamma_L = 12$  and the corresponding 2D case is only  $20$  s, which is less than  $5\%$ . This is a strong argument that 2D simulations can be used to investigate melting times with minimal loss of accuracy.

### 3.1.2. Comparison of 3D and 2D solid/liquid interfaces

To compare the 3D and 2D simulations in more detail, Fig. 5 (videos available as supplementary material) shows the evolution of the S/L interface for  $\Gamma_L = 6, 9$  and  $12$  with  $\Delta T = 40$  K, which is the largest value used. The shape of this interface is a consequence of the thermal distribution in the liquid phase and the rate at which warm liquid is carried to the front from the hot boundary. As mentioned above, the inclination of this front is a consequence of the accelerated heat transfer due to thermocapillary flow near the free surface. However, even with this high value of  $\Delta T$ , the transverse flow does not appreciably deform the S/L front during most of the melting process; small but growing wavy

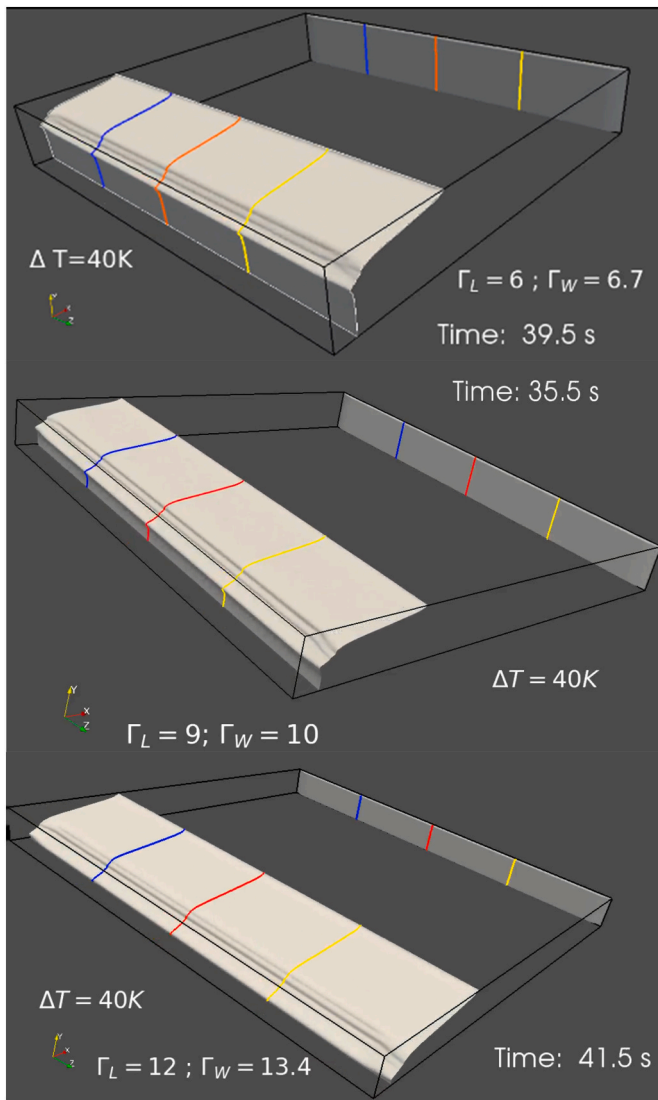


**Fig. 5.** Evolution of the S/L interface for  $\Delta T = 40$  K and several different aspect ratios. To better visualize the shape of the S/L front, colored lines show intersections with the planes  $z = 0$  and  $z = \pm W/4$ .

features can be seen near the bottom of the domain as time goes on.

### 3.1.3. Comparison of 3D and 2D thermal fields

A detailed comparison of the thermal fields obtained with the 2D and 3D simulations is provided in Fig. 6, which shows their complete evolution during the melting process for  $\Gamma_L = 6$  and  $\Delta T = 40$  K (largest  $H$  and thermal forcing) and for  $\Gamma_L = 12$  and  $\Delta T = 20$  K (smallest  $H$  and thermal forcing). The 3D results correspond to the central longitudinal plane at  $z = 0$ . In general, the observed thermal fields are in good agreement with previously published 2D results [18–20,31] and show how the thermocapillary flow in the vicinity of the free surface stretches and turns the initially vertical isotherms as it transports heat longitudinally and melts the upper layer of PCM.

At a certain point in both the 2D and 3D simulations, the isotherms begin to oscillate due to the appearance of hydrothermal waves. For  $\Gamma_L = 6$ , these oscillations are initially most vigorous near the hot boundary and resemble the oscillatory standing wave mode [20,62]. For  $\Gamma_L = 12$ , the oscillations are relatively more extended in  $x$  and have a more evident traveling wave character. However, as noted earlier, pure traveling waves are not possible with these boundary conditions and the oscillatory modes in both cases are mixed, with more of a modulated

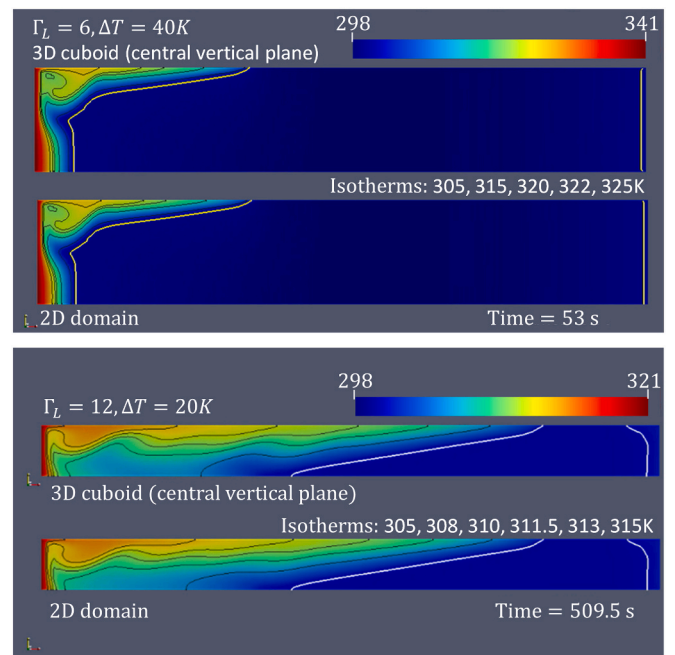


**Fig. 6.** Simultaneous evolution of thermal fields in 3D (central longitudinal plane) and 2D for (a)  $\Gamma_L = 6$ ,  $\Delta T = 40$  K and  $\Gamma_W = 6.67$  (3D case), (b)  $\Gamma_L = 12$ ,  $\Delta T = 20$  K and  $\Gamma_W = 13.33$  (3D case).

standing wave character near the surface (isotherms moving back and forth) and more of a traveling wave character near the lower boundary or solid PCM. The direction of wave motion is always upstream, from the cold boundary towards the hot one.

It is notable that oscillatory flow begins earlier in the 3D case; hereafter, this onset is denoted by  $t_{\text{onset\_3D}}$ . With  $\Gamma_L = 12$  and  $\Delta T = 20$  K, oscillations appear at  $t_{\text{onset\_3D}} \simeq 0.36 t_{\text{end}}$  but are delayed until approximately  $0.48 t_{\text{end}}$  in the 2D simulations. For  $\Gamma_L = 9$  and  $\Delta T = 30$  K (not shown in the figure), the oscillatory flow appears at  $t_{\text{onset\_3D}} \simeq 0.47 t_{\text{end}}$  but is delayed until  $0.86 t_{\text{end}}$  in the 2D model. The corresponding delay for  $\Gamma_L = 6$  and  $\Delta T = 40$  K is from  $t_{\text{onset\_3D}} \simeq 0.08 t_{\text{end}}$  to  $0.25 t_{\text{end}}$  in the 2D case. This delay is consistent with the fact that the classical hydrothermal traveling wave instability [34] is oblique; the waves are approximately streamwise for large  $Pr$ , but not exactly so. The 3D simulations permit this optimal oblique wavevector (or, at least, one closer to it) for hydrothermal waves while the 2D simulations can only capture streamwise wavevectors, which are associated with a higher threshold.

### 3.2. Spectral content

To quantitatively describe the behavior of the melting PCM, it is important to measure the spectral content of the dynamics. The analysis here is based on thermal signals taken from a point located in the central vertical plane at  $(x, y, z) = (0.1L, 0.95H, 0)$  with a sampling frequency of 2 Hz. Spectrograms are calculated using Hamming windows with 50% overlappings. Because the short-time Fourier transform uses 2048 points, the frequency resolution in all cases is approximately 1 mHz. Note that, since the signals associated with high  $\Delta T$  values (particularly,  $\Delta T = 40$  K) and rapid melting are shorter, the spectral analysis of these cases is more difficult [63–66].

Fig. 7 shows the results obtained for  $\Gamma_L = 6, 9$  and  $12$  and the same intermediate temperature difference  $\Delta T = 30$  K. The evolution of the temperature signal during the simulation can be seen along with an inset showing more detail of the thermal oscillations used to compute the spectrogram and the power spectral density. The qualitative behavior is similar in all cases, with an initial period during which the temperature rises smoothly followed by another one in which oscillations appear.

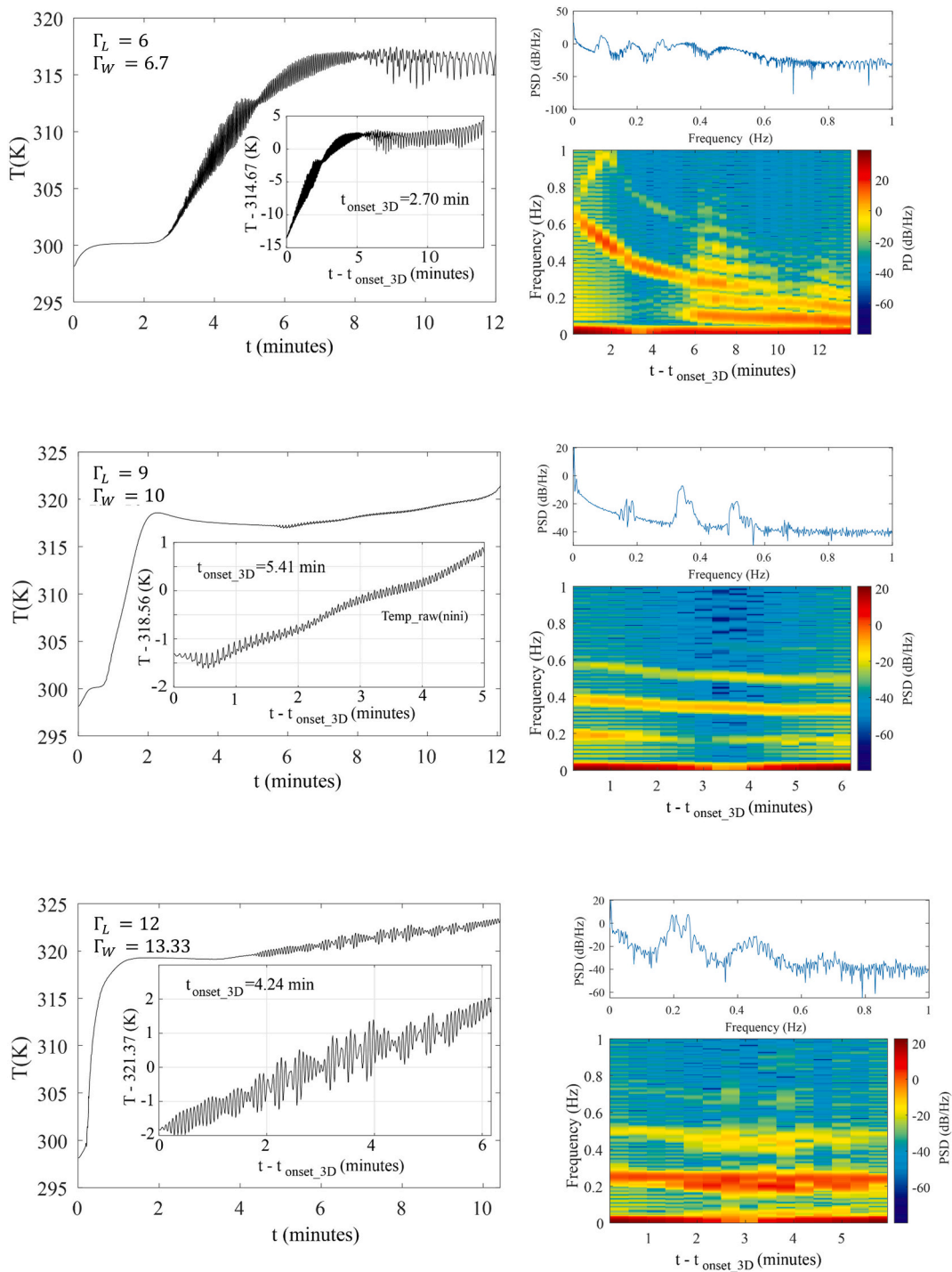


**Fig. 7.** 3D simulations. Temperature signal (left column) from the point  $(0.1L, 0.95H, 0)$  for  $\Delta T = 30$  K and three aspect ratios. To the right of each plot are the power spectral density (PSD) over the full interval of oscillations,  $t > t_{onset\_3D}$ , and a spectrogram showing the evolution of the PSD over a moving temporal window.

The oscillations are quantitatively characterized in the spectrograms, which reveal the frequency content between 0 and 1 Hz; since the sampling rate is 2 Hz, Nyquist's theorem means that higher frequencies are not resolved.

It is interesting to note the increasing complexity in these spectrograms as  $\Gamma_L$  decreases. For  $\Gamma_L = 12$ , a well-defined band near 0.23 Hz with a bandwidth of approximately 0.1 Hz is observed throughout the supercritical (oscillatory) regime of the melting process. The first harmonic frequency and a weaker band corresponding to the second harmonic can also be observed. The frequencies of these bands decrease in a barely perceptible manner during melting. The behavior is similar for

$\Gamma_L = 9$ , with a well-defined band around near 0.2 Hz having a bandwidth of about 0.1 Hz; the first and second harmonics are located near 0.4 and 0.6 Hz, respectively. With this aspect ratio, the decrease in frequency during melting is also quite mild. An approximately constant frequency of oscillatory flow is consistent with the hydrothermal traveling wave instability observed in the 2D case [20,31].

The situation for  $\Gamma_L = 6$ , however, is different. There is a significant decrease of the main frequency band (again with a bandwidth of approximately 0.1 Hz) from nearly 0.7 Hz to about 0.3 Hz over the first six minutes of melting. After that, as the S/L front near the free surface reaches the cold boundary at  $x = L$ , the frequency decrease slows while

another band centered at 0.1 Hz appears, along with its harmonics centered at 0.2, 0.3, 0.4 Hz, etc. This increase in height to  $H = 3.75$  mm for  $\Gamma_L = 6$  leads to a qualitative change in the character of the initial oscillatory convection that recalls the oscillatory standing wave mode observed in 2D simulations [20,31]. The subsequent period of oscillatory flow, after the primary frequency jumps to 0.1 Hz and then decreases much more slowly, is indicative of a transition to a type of hydrothermal traveling wave mode, as seen with the other two  $\Gamma_L$  values.

### 3.2.1. Comparison of 3D and 2D spectrograms

Again, we use the thermal signal from the point  $(x, y, z) = (0.1L, 0.95H, 0)$  in the central longitudinal plane to determine the spectral contents of the thermocapillary dynamics, and to compare the 3D and 2D cases. Fig. 8 shows several 3D and 2D spectrograms for the oscillatory thermal signals. We analyze the two temperature conditions  $\Delta T = 20$  K and  $\Delta T = 40$  K. As in the preceding case, the spectrograms start when the oscillations appear in the 3D case ( $t_{\text{onset\_3D}}$ ).

For  $\Delta T = 20$  K, the spectra are dominated by bands at low frequencies: approximately 0.05 Hz for  $\Gamma_L = 6$ , 0.1 Hz for  $\Gamma_L = 9$ , and 0.2 Hz for  $\Gamma_L = 12$ . The bandwidth is always about 0.1 Hz. The rest of the frequencies are harmonics of lower intensity.

For  $\Delta T = 40$  K, the spectral contents strongly depend on the aspect ratio. When  $\Gamma_L = 6$ , there is a higher-frequency band (starting near 1 Hz in the 3D case) that decreases to approximately 0.3 Hz; its lower-intensity first harmonic is also visible. Then, for the final few minutes

of the simulation, the 0.3 Hz band disappears (earlier in 3D than in 2D), leaving a nearly constant low-frequency band at approximately 0.05 Hz. This change is suggestive of a transition from oscillatory standing waves to hydrothermal traveling waves [31]. When  $\Gamma_L = 9$ , there is much greater discrepancy between the 3D and 2D simulations; only the frequency band near 0.5 Hz is common to both, and only for the initial period of oscillatory flow. Finally, when  $\Gamma_L = 12$ , there is a common frequency band near 0.2 Hz that decreases slightly over time, together with its harmonics.

In summary, the main spectral difference in most cases is that the hydrothermal waves appear earlier in the 3D simulations than in the 2D case. Nonetheless, the oscillatory regime is characterized by similar frequencies with similar dependence on time (melting) and on aspect ratio. This is evidence that, other than a delayed threshold, the 2D simulations capture the time dependence of the oscillatory modes reasonably well.

### 3.3. Transverse dynamics

Here, we characterize the transverse dynamics of the oscillatory modes in more detail. Fig. 9 shows the temporal evolution of the temperature field along the line segment defined by  $x = L/4, y = 0.95H$  and  $|z| \leq W/2$  after the appearance of oscillatory flow. This transverse line segment is close to the hot side and to the free surface, a suitable position to reveal transverse temperature fluctuations in space and time since they are not obscured by longitudinal fluctuations.

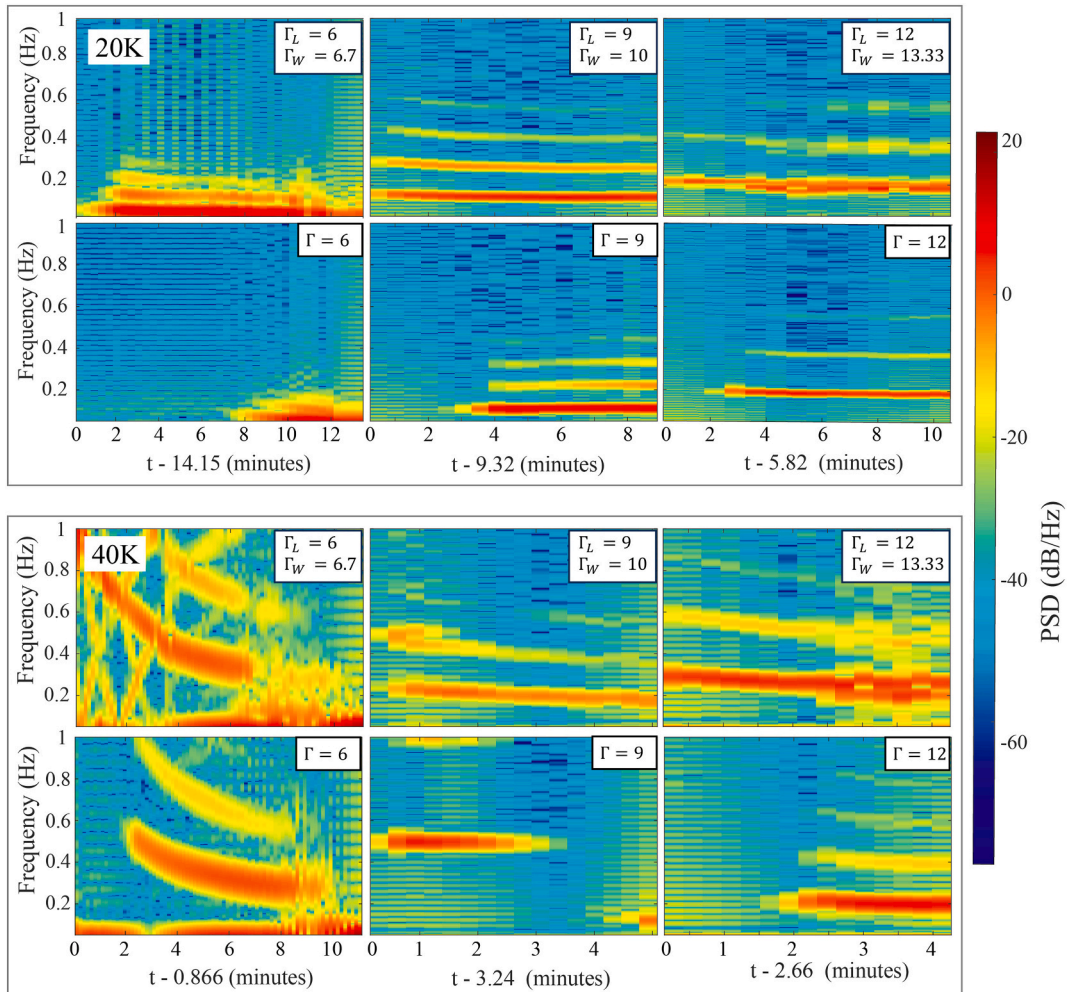
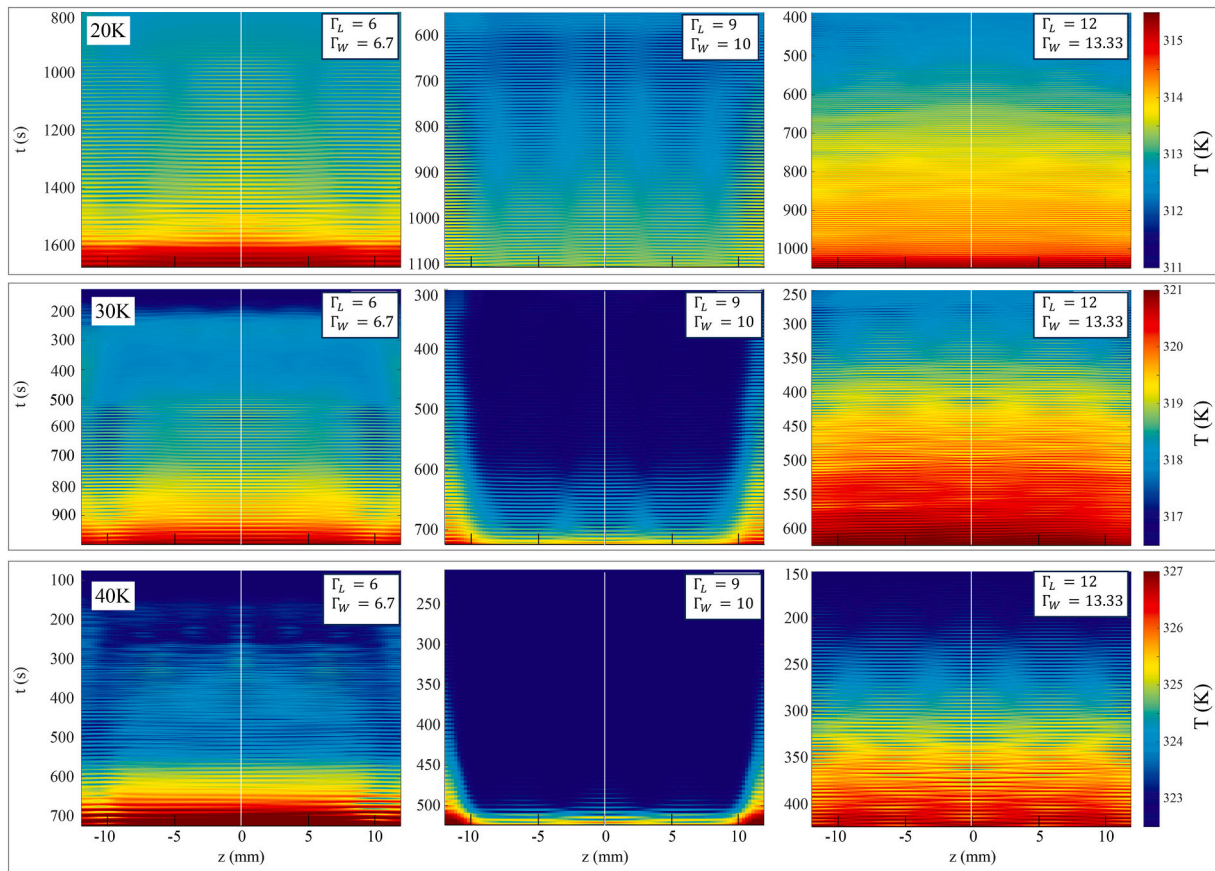


Fig. 8. Spectrograms of the temperature signal from the point  $(0.1L, 0.95H, 0)$  for  $\Delta T = 20$  K (upper block) and  $\Delta T = 40$  K (lower block) and for three aspect ratios. In each case, the 3D results (upper) are compared with the corresponding 2D simulations (lower).



**Fig. 9.** Space-time plots of the temperature signal along the line  $(L/4, 0.95H, z)$  for  $\Delta T = 20$  K (upper row),  $\Delta T = 30$  K (middle row) and  $\Delta T = 40$  K (lower row) for three aspect ratios. The color scale is the same across each row.

The upper row of Fig. 9 shows space-time plots with the temperature difference  $\Delta T = 20$  K for each of the three aspect ratios. The center row contains the same for  $\Delta T = 30$  K and the bottom row for  $\Delta T = 40$  K. The transverse component of the hydrothermal waves in these various cases is evident. Aside from the variation in onset of oscillations, there are differences in the transverse mode number. Many of the hydrothermal waves exhibit two full wavelengths in  $z$  (four nodes), but there are cases with one wavelength ( $\Gamma_L = 6$  and  $\Delta T = 20$  or 30 K) and with three ( $\Gamma_L = 6$  and  $\Delta T = 40$  K).

Considerable complexity and variation along the melting process can be observed with  $\Gamma_L = 12$  and with  $\Gamma_L = 6$  and  $\Delta T = 40$  K. However, in all cases, the modes are predominantly standing (i.e., reflection symmetric under  $z \rightarrow -z$ ). As noted with regard to Fig. 3, asymmetric transverse dynamics do sometimes appear near the end of melting and, upon close inspection, such symmetry-breaking can be seen with  $\Gamma_L = 6$  and  $\Delta T = 40$  K and with  $\Gamma_L = 12$  and  $\Delta T = 30$  K.

To complete the characterization of the transverse thermocapillary patterns, we show the thermal field in the plane  $y = 0.95H$ , which is located near the free surface. Its evolution for  $\Delta T = 40$  K is presented in Fig. 10 for the same three aspect ratios. In all cases, there is an initial period of time during which the S/L interface moves away from the hot boundary and the isotherms in the liquid phase are (almost) straight lines parallel to this wall. The duration of this period decreases with increasing aspect ratio.

The early quasi-steady dynamics gives way at some point to a more complex unsteady pattern whose properties depend on the aspect ratio. The most complex oscillatory dynamics are seen in the case of  $\Gamma = 6$  and  $\Delta T = 40$  K. While these dynamics preserve the  $z$ -reflection symmetry for a while, the symmetry is broken after approximately 400 s and an increasingly asymmetric transverse mode characterizes the remainder of

the melting process. For the other two aspect ratios, the oscillatory transverse modes remain symmetric throughout melting when  $\Delta T = 40$  K.

#### 4. Conclusions

Careful 3D simulations of thermocapillary-driven PCM melting in a cuboidal domain in microgravity conditions were performed in order to examine the effect of transverse dynamics and quantify any associated discrepancies with respect to the results of a simplified 2D model. Although the high Prandtl number of organic PCMs like n-octadecane partly justifies an assumption of 2D dynamics, 3D effects due to the lateral walls are invariably present in a real PCM. Here we find that the 2D model is, nonetheless, working reasonably well in capturing the essential properties of PCM melting dynamics.

The melting rates observed over time in the 3D and 2D simulations were seen to be very similar, with the same features associated, for instance, with the arrival of the solid/liquid front to the cold boundary. The total melting times typically differ by about 5% or less.

The evolution of the solid/liquid front was compared in the 2D and 3D models and found to behave similarly, especially when the central longitudinal plane is used for this comparison. At some point during the 3D simulations, however, visible undulations appear in the transverse direction and grow in amplitude, indicating the increasing importance of 3D effects near the end of the phase change.

The thermal fields were also compared in the 3D and 2D cases, and spectrograms were obtained from the thermal signal of a particular point near the surface by the hot wall. The thermal fields were seen to behave in analogous fashion, with comparable spectral content after the onset of oscillations, which suggests that the character of the thermocapillary

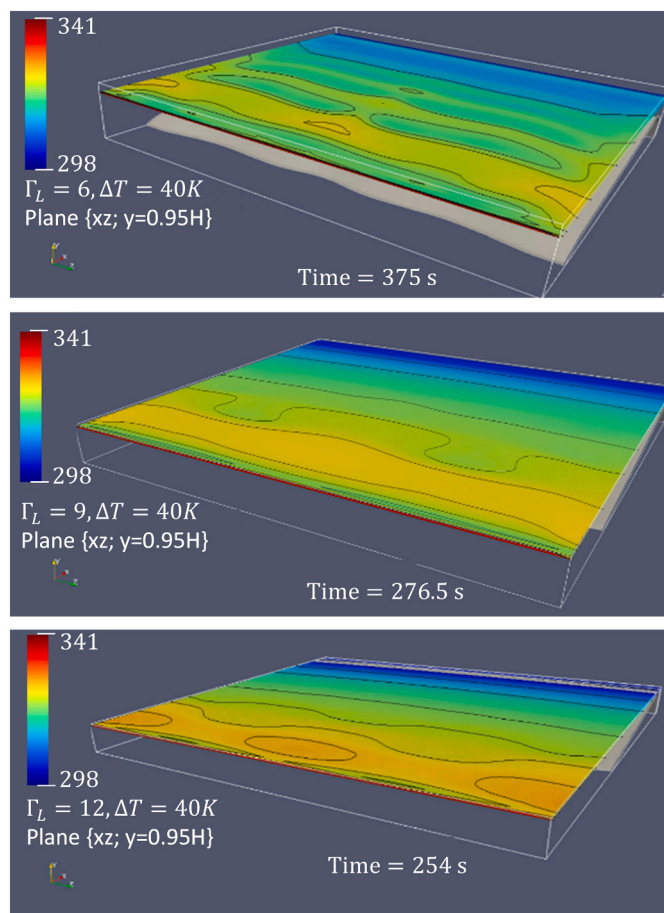


**Fig. 10.** Temperature distribution in the horizontal plane  $y = 0.95H$  near the free surface.

modes is well-captured by the 2D model. The most notable difference is the delayed onset of oscillatory dynamics in the 2D case. As mentioned above, this is consistent with the fact that the most dangerous mode for hydrothermal waves has a slightly oblique wavevector.

The nature of the transverse dynamics was examined and it was found that the hydrothermal mode at the onset of oscillations is typically reflection symmetric. In many simulations, this transverse standing mode corresponds to approximately two full wavelengths (four nodes), although one and three wavelengths can also be observed, depending on parameters. The reflection symmetry of the transverse modes is lost in a minority of cases as melting progresses, leading to more complex, asymmetric dynamics.

In summary, the 2D model reflects quite well the main features of the melting process for high Prandtl number PCMs like n-octadecane. Aside from a noticeable delay in the onset of hydrothermal waves, there are only minor quantitative deviations from the results of the full 3D simulations. Nonetheless, the increasing importance of 3D effects as melting progresses and the potential for complicated asymmetric transverse dynamics represent interesting topics for further investigation.

Supplementary data to this article can be found online at <https://doi.org/10.1016/j.icheatmasstransfer.2023.107198>.

Credit author statement.

**Berín Šeta:** Conceptualization, Methodology, Software, Writing –Original draft preparation, Writing-Reviewing and Editing **Pablo Salgado Sanchez:** Conceptualization, Investigation, Writing-Reviewing and Editing **Diana Dubert:** Visualization, Investigation, Data Curation **Jaume Massons:** Visualization, Investigation, Formal Analysis **Fina Gavalda:** Software, Visualization, Writing –Original draft preparation **Jeff Porter:** Writing –Original draft preparation, Investigation,

Writing-Reviewing and Editing, Project administration **M. Mounir Bou Ali:** Investigation, Funding acquisition, Supervision **Xavier Ruiz:** Writing –Original draft preparation, Investigation, Supervision, Software, Writing-Reviewing and Editing **Valentina Shevtsova:** Writing –Original draft preparation, Investigation, Formal Analysis, Supervision, Writing-Reviewing and Editing.

#### Declaration of Competing Interest

The authors declare that they have no known competing financial interests or personal relationships that could have appeared to influence the work reported in this paper.

#### Data availability

Data will be made available on request.

#### Acknowledgements

The present work has been supported by grants PID2020-115086GB-C32 and 2021PFR-URV-74. The work of P.S.S. and J.P. was supported by the Ministerio de Ciencia e Innovación under Project No. PID2020-115086GB-C31, and by the Spanish User Support and Operations Centre (E-USOC), Center for Computational Simulation (CCS). M.M.B. and V.S. was supported by the Ministerio de Ciencia e Innovación under Project No. PID2020-115086GB-C33, the Gipuzkoa Provincial Council under the Hoztikor project (2022-CIEN-000052-01) and KK-2023/00041 (MMASINT) KK-2023/00041 of the Basque Government.

#### References

- [1] R. Kandasamy, X.-Q. Wang, A.S. Mujumdar, Application of phase change materials in thermal management of electronics, *Appl. Therm. Eng.* 27 (2007) 2822–2832.
- [2] N. Chaiyat, T. Kiatsiriroat, Energy reduction of building air-conditioner with phase change material in Thailand, *Case Stud. Therm. Eng.* 4 (2014) 175–186.
- [3] K.O. Lee, M.A. Medina, Using phase change materials for residential air conditioning peak demand reduction and energy conservation in coastal and transitional climates in the state of California, *Energ. Build.* 116 (2016) 69–77.
- [4] P.H. Biwole, P. Eclache, F. Kuznik, Phase change materials to improve solar panel's performance, *Energ. Build.* 62 (2013) 59–67.
- [5] C.J. Ho, B.-T. Jou, C.-M. Lai, C.-Y. Huang, Performance assessment of a BIPV integrated with a layer of water-saturated MEPCM, *Energ. Build.* 67 (2013) 322–333.
- [6] J. Hirsche, K.R. Gluesenkamp, A. Mallow, S. Graham, Review of inorganic salt hydrates with phase change temperature in range of 5 °C to 60 °C and material cost comparison with common waxes, in: *proceedings of 5th international high performance buildings conference at Purdue*, July 9–12 (2018) 1–10.
- [7] F. Agyenim, P. Eames, M. Smyth, A comparison of heat transfer enhancement in a medium temperature thermal energy storage heat exchanger using fins, *Sol. Energy* 83 (2009) 1509–1520.
- [8] M. Medrano, M. Yilmaz, M. Nogués, I. Martorell, J. Roca, L.F. Cabeza, Experimental evaluation of commercial heat exchangers for use as pcm thermal storage systems, *Appl. Energy* 86 (2009) 2047–2055.
- [9] R. Koželj, E. Osterman, F. Leonforte, C. Del Pero, A. Miglioli, E. Zavri, R. Stropnik, N. Aste, U. Stritih, Phase-change materials in hydronic heating and cooling systems: a literature review, *Materials* 13 (2020).
- [10] A. Borschchak Kachalov, P. Salgado Sanchez, U. Martinez, J.M. Ezquerro, Preliminary design of a space habitat thermally controlled using phase change materials, *Thermo* 3 (2023) 232–247.
- [11] S.F. Hosseinzadeh, A.A.R. Darzi, F.L. Tan, Numerical investigations of unconstrained melting of nano-enhanced phase change material (NEPCM) inside a spherical container, *Int. J. Therm. Sci.* 51 (2012) 77–83.
- [12] N.S. Dhaidan, J.M. Khodadadi, T.A. Al-Hattab, S.M. Al-Mashat, Experimental and numerical investigation of melting of NePCM inside an annular container under a constant heat flux including the effect of eccentricity, *Int. J. Heat Mass Transf.* 67 (2013) 455–468.
- [13] C. Gau, R. Viskanta, Melting and solidification of a pure metal on a vertical wall, *Trans. ASME* 108 (1986) 174–181.
- [14] S.K. Roy, S. Sengupta, Gravity-assisted melting in a spherical enclosure: effects of natural convection, *Int. J. Heat Mass Transf.* 33 (1990) 1135–1147.
- [15] Y. Wang, A. Amiri, K. Vafai, An experimental investigation of the melting process in a rectangular enclosure, *Int. J. Heat Mass Transf.* 42 (1999) 3659–3672.
- [16] J.M. Khodadadi, Y. Zhang, Effects of buoyancy-driven convection on melting within spherical containers, *Int. J. Heat Mass Transf.* 44 (2001) 1605–1618.
- [17] N.S. Dhaidan, J.M. Khodadadi, Melting and convection of phase change materials in different shape containers: a review, *Renew. Sust. Energ. Rev.* 43 (2015) 449–477.

- [18] P. Salgado Sanchez, J.M. Ezquerro, J. Porter, J. Fernandez, I. Tinao, Effect of thermocapillary convection on the melting of phase change materials in microgravity: experiments and simulations, *Int. J. Heat Mass Transf.* 154 (2020), 119717.
- [19] P. Salgado Sanchez, J.M. Ezquerro, J. Fernandez, J. Rodriguez, Thermocapillary effects during the melting of phase change materials in microgravity: heat transport enhancement, *Int. J. Heat Mass Transf.* 163 (2020), 120478.
- [20] P. Salgado Sanchez, J.M. Ezquerro, J. Fernandez, J. Rodriguez, Thermocapillary effects during the melting of phase change materials in microgravity: steady and oscillatory flow regimes, *J. Fluid Mech.* 908 (2021) A20.
- [21] N. Garcia-Acosta, P. Salgado Sanchez, J. Jimenez, U. Martinez, J.M. Ezquerro, Thermocapillary-enhanced melting of different phase-change materials in microgravity, *Microgr. Sci. Technol.* 34 (2022) 92.
- [22] A. Borshchak Kachalov, R. Garcia-Roco, P. Salgado Sanchez, K. Olfe, A. Bello, Thermocapillary effects during the melting of phase change materials subjected to lateral heat flux in microgravity, *Int. J. Heat Mass Transf.* 218 (2024), 124806.
- [23] S. Madruga, C. Mendoza, Enhancement of heat transfer rate on phase change materials with thermocapillary flows, *Europ. Phys. J. Spec. Top.* 226 (2017) 1169–1176.
- [24] S. Madruga, C. Mendoza, Heat transfer performance and melting dynamic of a phase change material subjected to thermocapillary effects, *Int. J. Heat Mass Transf.* 109 (2017) 501–510.
- [25] J.M. Ezquerro, A. Bello, P. Salgado Sanchez, A. Laveron-Simavilla, V. Lapuerta, The Thermocapillary effects in phase change materials in microgravity experiment: design, preparation and execution of a parabolic flight experiment, *Acta Astronaut.* 162 (2019) 185–196.
- [26] J.M. Ezquerro, P. Salgado Sanchez, A. Bello, J. Rodriguez, V. Lapuerta, A. Laveron-Simavilla, Experimental evidence of thermocapillarity in phase change materials in microgravity: measuring the effect of marangoni convection in solid/liquid phase transitions, *Int. Commun. Heat Mass Transf.* 113 (2020), 104529.
- [27] R. Varas, P. Salgado Sanchez, J. Porter, J.M. Ezquerro, V. Lapuerta, Thermocapillary effects during the melting in microgravity of phase change materials with a liquid bridge geometry, *Int. J. Heat Mass Transf.* 178 (2021), 121586.
- [28] B. Šeta, D. Dubert, J. Massons, J. Gavalda, M.M. Bou-Ali, X. Ruiz, Effect of marangoni induced instabilities on a melting bridge under microgravity conditions, *Int. J. Heat Mass Transf.* 179 (2021), 121665.
- [29] A. Borshchak Kachalov, P. Salgado Sánchez, U. Martínez, J. Fernández, J. M. Ezquerro, Optimization of thermocapillary-driven melting in trapezoidal and triangular geometry in microgravity, *Int. J. Heat Mass Transf.* 185 (2022), 122427.
- [30] N. Martínez, P. Salgado Sanchez, J. Porter, J.M. Ezquerro, Effect of surface heat exchange on phase change materials melting with thermocapillary flow in microgravity, *Phys. Fluids* 33 (2021), 083611.
- [31] P. Salgado Sanchez, J. Porter, J.M. Ezquerro, I. Tinao, A. Laveron-Simavilla, Pattern selection for thermocapillary flow in rectangular containers in microgravity, *Phys. Rev. Fluids* 7 (2022), 053502.
- [32] D. Schwabe, A. Scharmann, Some evidence for the existence and magnitude of a critical marangoni number of the onset of oscillatory flow in crystal growth melts, *J. Cryst. Growth* 46 (1979) 125–131.
- [33] A.K. Sen, S.H. Davis, Steady thermocapillary flows in two-dimensional slots, *J. Fluid Mech.* 121 (1982) 163–186.
- [34] M.K. Smith, S.H. Davis, Instabilities of dynamic thermocapillary liquid layers. Part 1. Convective instabilities, *J. Fluid Mech.* 132 (1983) 119–144.
- [35] M.K. Smith, Instability mechanisms in dynamic thermocapillary liquid layers, *Phys. Fluids* 29 (1986) 3182.
- [36] V. Shevtsova, A. Nepomnyashchy, J.C. Legros, Thermocapillary-buoyancy convection in a shallow cavity heated from the side, *Phys. Rev. E* 67 (2003), 066308.
- [37] B. Šeta, D. Dubert, J. Gavalda, J. Massons, M.M. Bou-Ali, X. Ruiz, V. Shevtsova, Effect of heat transfer through an interface on convective melting dynamics of phase change materials, *J. Fluid Mech.* 966 (2023) A46.
- [38] P. Salgado Sánchez, J.M. Ezquerro, D. Gligor, U. Martínez, J. Fernández, I. Tinao, The “effect of marangoni convection on heat transfer in phase change materials” experiment, from a student project to the international space station, in: *Proceedings of the 4th Symposium on Space Education Activities*, 2022, pp. 1–6.
- [39] J. Porter, A. Laverón-Simavilla, M. Bou-Ali, X. Ruiz, F. Gavalda, J. Ezquerro, P. Salgado Sánchez, U. Martínez, D. Gligor, I. Tinao, J. Gómez, J. Fernández, J. Rodríguez, A.B. Kachalov, V. Lapuerta, B. Šeta, J. Massons, D. Dubert, A. Sanjuan, V. Shevtsova, L. García-Fernández, The “Effect of Marangoni Convection on Heat Transfer in Phase Change Materials” experiment, *Acta Astronautica* 210 (2023) 212–223.
- [40] A. Borshchak Kachalov, P. Salgado Sanchez, J. Porter, J.M. Ezquerro, The combined effect of natural and thermocapillary convection on the melting of phase change materials in rectangular containers, *Int. J. Heat Mass Transf.* 168 (2021), 120864.
- [41] R. Varas, U. Martinez, K. Olfe, P. Salgado Sánchez, J. Porter, J.M. Ezquerro, Effects of thermocapillary and natural convection during the melting of phase change materials with a liquid bridge geometry, *Microgr. Sci. Technol.* 35 (2023) 17.
- [42] B. Šeta, D. Dubert, J. Massons, P.S. Sánchez, J. Porter, J. Gavalda, M. Bou-Ali, X. Ruiz, On the Impact of Body Forces in Low Prandtl Number Liquid Bridges, Springer International Publishing, 2021, pp. 217–227.
- [43] B. Šeta, D. Dubert, M. Prats, J. Gavalda, J. Massons, M. Bou-Ali, X. Ruiz, V. Shevtsova, Transitions between nonlinear regimes in melting and liquid bridges in microgravity, *Int. J. Heat Mass Transf.* 193 (2022), 122984.
- [44] N. Martínez Figueira, P. Salgado Sanchez, A. Bello, K. Olfe, J. Rodriguez, Effect of surface heat exchange on phase change materials melting with thermocapillary flow in microgravity, *Phys. Fluids* 35 (2023), 084115.
- [45] S. Madruga, C. Mendoza, Heat transfer performance and thermal energy storage in nano-enhanced phase change materials driven by thermocapillarity, *Int. Commun. Heat Mass Transf.* 129 (2021), 105672.
- [46] D. Gligor, P. Salgado Sánchez, J. Porter, I. Tinao, Thermocapillary-driven dynamics of a free surface in microgravity: response to steady and oscillatory thermal excitation, *Phys. Fluids* 34 (2022), 042116.
- [47] D. Gligor, P. Salgado Sánchez, J. Porter, J. Ezquerro Navarro, Thermocapillary-driven dynamics of a free surface in microgravity: control of sloshing, *Phys. Fluids* 34 (2022), 072109.
- [48] P. Salgado Sanchez, U. Martinez, D. Gligor, I. Torres, J. Plaza, J.M. Ezquerro, The “thermocapillary-based control of a free surface in microgravity” experiment, *Acta Astronaut.* 205 (2023) 57–67.
- [49] C. Peromingo, D. Gligor, P. Salgado Sánchez, A. Bello, K. Olfe, Sloshing reduction in microgravity: thermocapillary-based control and passive baffles, *Phys. Fluids* 35 (2023), 102114.
- [50] C. Peromingo, P. Salgado Sánchez, D. Gligor, A. Bello, J. Rodriguez, Sloshing reduction in microgravity with passive baffles: design, performance, and supplemental thermocapillary control, *Phys. Fluids* 35 (11) (2023).
- [51] H.C. Kuhlmann, S. Albensoeder, Three-dimensional flow instabilities in a thermocapillary-driven cavity, *Phys. Rev. E* 77 (2008), 036303.
- [52] E.M. Alawadhi, Thermal analysis of a building brick containing phase change material, *Energ. Build.* 40 (2008) 351–357.
- [53] D.R. Lide, *Handbook of Chemistry and Physics*, 2014.
- [54] V.R. Voller, M. Cross, N.C. Markatos, An enthalpy method for convection/diffusion phase change, *Int. J. Numer. Methods Eng.* 24 (1987) 271–284.
- [55] A fixed grid numerical modelling methodology for convection-diffusion mushy region phase-change problems, *Int. J. Heat Mass Transf.* 30 (1987) 1709–1719.
- [56] C.R. Swaminathan, V.R. Voller, On the enthalpy method, *Int. J. Numer. Methods Heat Fluid Flow* 3 (1993) 233–244.
- [57] J.M. Montanero, C. Ferrero, V.M. Shevtsova, Experimental study of the free surface deformation due to thermal convection in liquid bridges, *Exp. Fluids* 45 (2008) 1087–1101.
- [58] V. Voller, A. Brent, C. Prakash, The modelling of heat, mass and solute transport in solidification systems, *Int. J. Heat Mass Transf.* 32 (1989) 1719–1731.
- [59] F.P. Kärholm, Rhie-Chow Interpolation in Openfoam, 2007.
- [60] S. Madruga, G.S. Mischlich, Melting dynamics of a phase change material (PCM) with dispersed metallic nanoparticles using transport coefficients from empirical and mean field models, *Appl. Therm. Eng.* 124 (2017) 1123–1133.
- [61] B. Šeta, P.S. Sánchez, J. Massons, J. Gavalda, J. Porter, M. Bou-Ali, X. Ruiz, V. Shevtsova, Three-dimensional effects during the melting of phase-change materials with thermocapillary flow in microgravity, in: *27th European Low Gravity Research Association Biennial Symposium*, Lisbon, 2022.
- [62] L.J. Peltier, S. Biringen, Time-dependent thermocapillary convection in a rectangular cavity: numerical results for a moderate Prandtl number fluid, *J. Fluid Mech.* 257 (1993) 339–357.
- [63] N. Sáez, J. Gavalda, X. Ruiz, V. Shevtsova, Detecting accelerometric nonlinearities in the international space station, *Acta Astronaut.* 103 (2014) 16–25.
- [64] J. Ollé, D. Dubert, J. Gavalda, A. Laverón-Simavilla, X. Ruiz, V. Shevtsova, Onsite vibrational characterization of DCMIX2/3 experiments, *Acta Astronaut.* 140 (2017) 409–419.
- [65] D. Dubert, J. Ollé, R. Jurado, J. Gavalda, A. Laverón-Simavilla, X. Ruiz, V. Shevtsova, Characterization of the accelerometric environment of DCMIX2/3 experiments, *Microgr. Sci. Technol.* 30 (2018) 683–697.
- [66] D. Dubert, M. Marín-Genescà, M.J. Simón, J. Ezquerro, J. Massons, J. Gavalda, X. Ruiz, V. Shevtsova, On the monitoring of the vibratory environment of DCMIX4 campaign. Preliminary results, *Microgr. Sci. Technol.* 32 (2020) 615–628.